A&A 560, A73 (2013)
DOI: 10.1051/0004-6361/201322460

Astronomy & Astrophysics

The IRAM-30 m line survey of the Horsehead PDR

IV. Comparative chemistry of H_2CO and CH_3OH⋆,⋆⋆

V. V. Guzmán[1], J. R. Goicoechea[2], J. Pety[1,3], P. Gratier[1], M. Gerin[3], E. Roueff[4], F. Le Petit[4], J. Le Bourlot[4], and A. Faure[5]

[1] Institut de Radioastronomie Millimétrique (IRAM), 300 rue de la Piscine, 38406 Saint-Martin-d'Hères, France
e-mail: [guzman;pety;gratier]@iram.fr
[2] Departamento de Astrofísica, Centro de Astrobiología, CSIC-INTA, Carretera de Ajalvir, Km 4. Torrejón de Ardoz, 28850 Madrid, Spain
e-mail: jr.goicoechea@cab.inta-csic.es
[3] LERMA – LRA, UMR 8112, Observatoire de Paris and École Normale Supérieure, 24 rue Lhomond, 75231 Paris, France
e-mail: maryvonne.gerin@lra.ens.fr
[4] LUTH UMR 8102, CNRS and Observatoire de Paris, Place J. Janssen, 92195 Meudon Cedex, France
e-mail: [evelyne.roueff;franck.lepetit;jacques.lebourlot]@obspm.fr
[5] UJF-Grenoble 1/CNRS-INSU, Institut de Planétologie et d'Astrophysique de Grenoble (IPAG) UMR 5274, 38041 Grenoble, France
e-mail: alexandre.faure@obs.ujf-grenoble.fr

Received 7 August 2013 / Accepted 21 October 2013

ABSTRACT

Context. Theoretical models and laboratory experiments show that CH_3OH is efficiently formed on cold grain surfaces through the successive hydrogenation of CO, forming HCO and H_2CO as intermediate species. In cold cores and low UV-field illumination photodissociation regions (PDRs) the ices can be released into the gas-phase through nonthermal processes such as photodesorption, which considerably increases their gas-phase abundances.
Aims. We investigate the dominant formation mechanism of H_2CO and CH_3OH in the Horsehead PDR and its associated dense core.
Methods. We performed deep integrations of several H_2CO and CH_3OH lines at two positions in the Horsehead, namely the PDR and dense core, with the IRAM-30 m telescope. In addition, we observed one H_2CO higher-frequency line with the CSO telescope at both positions. We determined the H_2CO and CH_3OH column densities and abundances from the single-dish observations complemented with IRAM-PdBI high-angular resolution maps (6″) of both species. We compared the observed abundances with PDR models including either pure gas-phase chemistry or both gas-phase and grain surface chemistry.
Results. We derived CH_3OH abundances relative to total number of hydrogen atoms of $\sim 1.2 \times 10^{-10}$ and $\sim 2.3 \times 10^{-10}$ in the PDR and dense-core positions, respectively. These abundances are similar to the inferred H_2CO abundance in both positions ($\sim 2 \times 10^{-10}$). We find an abundance ratio H_2CO/CH_3OH of ∼2 in the PDR and ∼1 in the dense core. Pure gas-phase models cannot reproduce the observed abundances of either H_2CO or CH_3OH at the PDR position. The two species are therefore formed on the surface of dust grains and are subsequently photodesorbed into the gas-phase at this position. At the dense core, on the other hand, photodesorption of ices is needed to explain the observed abundance of CH_3OH, while a pure gas-phase model can reproduce the observed H_2CO abundance. The high-resolution observations show that CH_3OH is depleted onto grains at the dense core. CH_3OH is thus present in an envelope around this position, while H_2CO is present in both the envelope and the dense core itself.
Conclusions. Photodesorption is an efficient mechanism to release complex molecules in low-FUV-illuminated PDRs, where thermal desorption of ice mantles is ineffective.

Key words. astrochemistry – ISM: clouds – ISM: molecules – photon-dominated region (PDR) – radiative transfer – radio lines: ISM

1. Introduction

Formaldehyde (H_2CO) and methanol (CH_3OH) are key species in the synthesis of more complex organic molecules, such as amino acids and other prebiotic molecules (Bernstein et al. 2002; Muñoz Caro et al. 2002; Garrod et al. 2008), that might finally arrive in proto-planetary disks, and hence in new planetary systems. It is therefore of great interest to understand how these molecules are formed. Both species have been detected in a wide range of interstellar environments, with typical gas-phase abundances relative to H_2 of $\sim 10^{-7}$ in hot cores (e.g., Sutton et al. 1995; Ceccarelli et al. 2000) and $\sim 10^{-9}$ in cold dark clouds (e.g., Bergman et al. 2011). They are also observed in shocked regions, caused by an impact of molecular outflows on the surrounding molecular clouds (e.g., Sakai et al. 2012; Codella et al. 2012; Tafalla et al. 2010). Because they are slightly asymmetric rotors, H_2CO and CH_3OH are good tracers of the physical conditions in Galactic and extragalactic molecular clouds (Mangum & Wootten 1993; Leurini et al. 2004; Mangum et al. 2013).

Unlike H_2CO, which can be formed both in the gas-phase and on the surface of dust grains, CH_3OH is thought to be formed entirely on the surfaces of dust grains, because classical

⋆ Based on observations obtained with the IRAM Plateau de Bure interferometer and 30 m telescope. IRAM is supported by INSU/CNRS (France), MPG (Germany), and IGN (Spain).
⋆⋆ The reduced datacubes (FITS files) are only available at the CDS via anonymous ftp to cdsarc.u-strasbg.fr (130.79.128.5) or via http://cdsarc.u-strasbg.fr/viz-bin/qcat?J/A+A/560/A73

Table 1. Observation parameters for the 30 m maps shown in Fig. 3.

Molecule	Transition	Frequency GHz	Instrument	Mode	Beam arcsec	Vel. resol. km s^{-1}	Int. time hours	T_{sys} K (T_A^*)	Noise K (T_{mb})	Reference
Continuum at 1.2 mm			30 m/MAMBO	–	11.7 × 11.7	–	–	–	–	Hily-Blant et al. (2005)
DCO^+	3–2	216.112582	30 m/HERA	FSW	11.4 × 11.4	0.11	1.5/2.0[a]	230	0.10	Pety et al. (2007)
p − H_2CO	3_{03}−2_{02}	218.222190	30 m/HERA	PSW	11.9 × 11.9	0.05	2.1/3.4[a]	280	0.32	Guzmán et al. (2011)
p − H_2CO	2_{02}−1_{01}	145.602949	30 m/EMIR	PSW	17.8 × 17.8	0.20	7.4/12.9[a]	208	0.17	This work
CH_3OH − E	3_{-1}−2_{-1}	145.097370	30 m/EMIR	PSW	17.9 × 17.9	0.20	7.4/12.9[a]	208	0.108[b]	This work
			30 m/C150	FSW	17.9 × 17.9	0.20	2.6/3.2[a]	163	0.108[b]	This work
CH_3OH − A	3_0−2_0	145.103152	30 m/EMIR	PSW	17.9 × 17.9	0.20	7.4/12.9[a]	208	0.095[b]	This work
			30 m/C150	FSW	17.9 × 17.9	0.20	2.6/3.2[a]	263	0.095[b]	This work

Notes. The projection center of the maps is $\alpha_{2000} = 05^h40^m54.27^s$, $\delta_{2000} = -02°28'00''$. [(a)] Two values are given for the integration time: the on-source time and the telescope time. [(b)] The noise value is computed on the final maps that combine the data from both observing runs (2007 and 2012).

ion-neutral chemistry in the gas-phase alone cannot account for the observed CH_3OH abundances (Garrod et al. 2006; Geppert et al. 2006). The mechanism to form CH_3OH on ices is thought to be the successive hydrogenation of CO, forming H_2CO as an intermediate product,

$$CO \xrightarrow[H]{E_b} HCO \underset{H}{\rightarrow} H_2CO \xrightarrow[H]{E_b} CH_2OH, CH_3O \underset{H}{\rightarrow} CH_3OH, \quad (1)$$

where E_b are activation energy barries (Tielens & Whittet 1997; Watanabe & Kouchi 2002). Indeed, laboratory experiments have succeeded to efficiently form both H_2CO and CH_3OH through this mechanism (Watanabe et al. 2004; Fuchs et al. 2009). Moreover, observations by the Infrared Space Observatory (ISO) and *Spitzer* have shown that dust grains are covered by ice mantles in the cold envelopes surrounding high-mass protostars (Gibb et al. 2000, 2004), low-mass protostars (Boogert et al. 2008; Pontoppidan et al. 2008; Öberg et al. 2008; Bottinelli et al. 2010), and in isolated dense cores (Boogert et al. 2011). These studies revealed that the ice mantles consist mostly of H_2O, CO_2 and CO, with smaller amounts of CH_3OH, CH_4, NH_3, and H_2CO. HCO ice has not been detected in the interstellar medium (ISM), probably because its formation on the ices is slower than its subsequent hydrogenation to form H_2CO. Indeed, the reactions starting with CO and H_2CO in the hydrogenation path (1) have activation energy barriers (Fuchs et al. 2009).

Once these species are formed on the ices, they can be desorbed into the gas-phase either through thermal or nonthermal processes. Thermal desorption dominates in regions where dust grains reach temperatures of at least 45 K for formaldehyde (Tielens & Allamandola 1987) and 80 K for methanol (Brown & Bolina 2007; Green et al. 2009). This occurs in hot cores and hot corinos (e.g., Jørgensen et al. 2005; Bisschop et al. 2007; Bottinelli et al. 2007), but also in highly far-ultraviolet (FUV) illuminated photo-dissociation regions (PDRs), such as the Orion bar (Leurini et al. 2010). Nonthermal desorption by FUV photons can also be efficient, as shown by laboratory experiments (Öberg et al. 2009b,c). Nonthermal desorption dominates in colder regions, either UV-shielded dense cores where secondary UV photons are produced by the interaction between cosmic rays and H_2 molecules (e.g., Caselli et al. 2012), or in low-UV-field illumination photo-dissociation regions, where dust grains are too cold to sublimate their ices. This is the case of the Horsehead, where the combination of a moderate-radiation field ($\chi = 60$ relative to the Draine field; Draine 1978), and high density ($n_H \sim 10^4$–10^5 cm^{-3}) implies low dust grain temperatures, from $T_{dust} \sim 30$ K in the outer PDR to $T_{dust} \sim 20$ K slightly deeper inside the cloud (Goicoechea et al. 2009a). Guzmán et al. (2011) compared single-dish observations of H_2CO with PDR models including grain-surface chemistry. They showed that the observed H_2CO abundance in the UV-illuminated edge of the Horsehead nebula can only be explained by the formation of H_2CO on the grains followed by its photo-desorption into the gas-phase. Pure gas-phase chemistry was enough to explain the H_2CO abundance in the colder and UV-shielded gas. The assignments of different formation routes were strengthened by the different measured ortho-to-para ratio of H_2CO: the dense core displays an equilibrium value of ∼3, while the PDR displays an out-of-equilibrium value of ∼2. The PDR model predicted that H_2CO will be one order of magnitude more abundant in the PDR than the IRAM-30 m beam-averaged measurements.

To further constrain the chemistry of complex organic molecules and investigate the high abundance in the PDR position predicted by the model, we here present high-resolution interferometric maps of H_2CO and CH_3OH in addition to single-dish deep integrations of the low-lying rotational lines of CH_3OH toward two particular positions in the Horsehead: the warm PDR and its associated cold dense core. The observations and data reduction are presented in Sect. 2. The resulting single-dish and interferometric data are described in Sect. 3. In Sect. 4, we compute the CH_3OH column densities and abundances. We compare these results with PDR models in Sect. 5. A discussion is presented in Sect. 6. We summarize and conclude in Sect. 7.

2. Observations and data reduction

In this section, we describe the observations and data reduction of the newly acquired H_2CO and CH_3OH data. A detailed description of the HCO, 218.222 GHz H_2CO, DCO^+, and 1.2 mm continuum observations and data reduction can be found in Gerin et al. (2009), Guzmán et al. (2011), Pety et al. (2007), and Hily-Blant et al. (2005), respectively. Tables 1–3 summarize the observation parameters of the data obtained with the IRAM-30 m, PdBI, and CSO telescopes.

2.1. PdBI maps

We used the Plateau de Bure Interferometer (PdBI) to obtain 6″ resolution maps of the emission of the H_2CO 2_{02}−1_{01} line at 146.603 GHz, the CH_3OH − E 3_{-1}−2_{-1} line at 145.097 GHz, and the CH_3OH − A 3_0−2_0 line at 145.103 GHz. These observations were carried out in August and October 2011 with five

Table 2. Observation parameters for the PdBI maps shown in Fig. 4.

Molecule	Transition	Frequency GHz	Instrument	Beam arcsec	PA °	Vel. resol. km s^{-1}	Int. time hours	T_{sys} K (T_A^*)	Noise mK (T_{mb})	Reference
HCO	1_{01} 3/2, 2–0_{00} 1/2, 1	86.670760	PdBI/C&D	6.7 × 4.4	16	0.20	6.5[a]	150	90[b]	Gerin et al. (2009)
p – H_2CO	2_{02}–1_{01}	145.602949	PdBI/C&D	6.1 × 5.6	166	0.20	5.3/19[a]	145	244	This work
CH_3OH – E	3_{-1}–2_{-1}	145.097370	PdBI/C&D	6.1 × 5.6	166	0.20	5.3/19[a]	145	116	This work
CH_3OH – A	3_0–2_0	145.103152	PdBI/C&D	6.1 × 5.6	166	0.20	5.3/19[a]	145	127	This work

Notes. The projection center of the maps is $\alpha_{2000} = 05^h40^m54.27^s$, $\delta_{2000} = -02°28'00''$. [(a)] Two values are given for the integration time: the on-source time (as if the source were always observed with 6 antennae) and the telescope time. [(b)] The noise values quoted here are the noises at the mosaic phase center (mosaic noise is inhomogeneous due to primary-beam correction; it steeply increases at the mosaic edges).

Table 3. Observation parameters of the deep integrations of the CH_3OH lines detected with the 30 m and the H_2CO line detected with the CSO toward the PDR and the dense core.

Position	Molecule	Transition	ν GHz	Line area mK km s^{-1}	Velocity km s^{-1}	*FWHM* km s^{-1}	T_{peak} mK	rms mK	*S/N*
PDR	CH_3OH – E	5_{-1}–4_0	84.521	29.1 ± 3.1	10.64 ± 0.05	0.98 ± 0.14	27.9	4.7	6
	CH_3OH – E	2_{-1}–1_{-1}	96.739	74.1 ± 4.3	10.73 ± 0.02	0.56 ± 0.04	125.0	9.4	13
	CH_3OH – E	2_0–1_0	96.745	22.3 ± 4.7	10.68 ± 0.05	0.63 ± 0.21	33.2	7.5	4
	CH_3OH – E	3_0–2_0	145.094	26.9 ± 6.5	10.77 ± 0.05	0.42 ± 0.11	59.8	21.7	3
	CH_3OH – E	3_{-1}–2_{-1}	145.097	98.4 ± 9.0	10.54 ± 0.02	0.51 ± 0.06	180.8	21.5	8
	CH_3OH – E	5_{-1}–4_{-1}	241.767	81.0 ± 8.8	10.66 ± 0.04	0.85 ± 0.11	89.5	13.1	7
	CH_3OH – A	2_0–1_0	96.741	120.3 ± 3.9	10.73 ± 0.01	0.61 ± 0.02	186.6	7.7	24
	CH_3OH – A	3_0–2_0	145.103	145.7 ± 7.0	10.66 ± 0.01	0.51 ± 0.03	266.2	19.4	14
	CH_3OH – A	5_0–4_0	241.791	59.5 ± 7.3	10.81 ± 0.03	0.48 ± 0.08	117.1	12.5	9
	o-H_2CO	4_{13}–3_{12}	300.837	204.1 ± 39.0	10.75 ± 0.07	0.68 ± 0.16	281.1	60.8	5
Core	CH_3OH – E	5_{-1}–4_0	84.521	43.8 ± 3.0	10.64 ± 0.02	0.65 ± 0.05	63.3	6.4	10
	CH_3OH – E	2_{-1}–1_{-1}	96.739	304.4 ± 3.5	10.65 ± 0.00	0.57 ± 0.01	497.5	7.9	63
	CH_3OH – E	2_0–1_0	96.745	57.6 ± 2.7	10.66 ± 0.01	0.50 ± 0.03	107.6	5.7	19
	CH_3OH – E	2_1–1_1	96.755	11.0 ± 3.0	10.56 ± 0.05	0.41 ± 0.14	25.0	7.0	3
	CH_3OH – E	0_0–1_{-1}	108.894	74.4 ± 4.6	10.63 ± 0.01	0.46 ± 0.03	151.8	13.5	11
	CH_3OH – E	3_0–2_0	145.094	50.4 ± 6.9	10.48 ± 0.02	0.31 ± 0.05	154.5	24.3	6
	CH_3OH – E	3_{-1}–2_{-1}	145.097	449.7 ± 7.5	10.48 ± 0.00	0.52 ± 0.01	819.8	21.6	38
	CH_3OH – E	3_1–2_1	145.132	<12	–	0.5[a]	–	22.0	–
	CH_3OH – E	1_0–1_{-1}	157.271	122.3 ± 11.0	10.66 ± 0.03	0.56 ± 0.05	206.9	34.8	6
	CH_3OH – E	2_0–2_{-1}	157.276	69.5 ± 9.7	10.64 ± 0.03	0.42 ± 0.07	154.0	28.1	5
	CH_3OH – E	1_1–0_0	213.427	42.8 ± 6.4	10.64 ± 0.04	0.46 ± 0.07	87.5	12.2	7
	CH_3OH – E	4_2–3_1	218.440	47.4 ± 5.6	10.62 ± 0.04	0.62 ± 0.08	71.5	9.2	8
	CH_3OH – E	5_{-1}–4_{-1}	241.767	170.8 ± 7.9	10.57 ± 0.01	0.52 ± 0.03	311.5	15.3	20
	CH_3OH – E	2_0–1_{-1}	254.015	59.6 ± 4.3	10.53 ± 0.02	0.44 ± 0.03	126.5	7.9	16
	CH_3OH – E	2_1–1_0	261.806	43.3 ± 7.3	10.56 ± 0.03	0.29 ± 0.14	141.1	22.5	6
	CH_3OH – A	2_0–1_0	96.741	448.5 ± 3.9	10.65 ± 0.00	0.58 ± 0.01	725.6	8.1	89
	CH_3OH – A	3_0–2_0	145.103	527.2 ± 8.0	10.56 ± 0.00	0.52 ± 0.01	949.5	21.3	45
	CH_3OH – A	5_0–4_0	241.791	200.2 ± 8.9	10.67 ± 0.01	0.47 ± 0.02	398.4	16.2	25
	o-H_2CO	4_{13}–3_{12}	300.837	211.1 ± 33.0	10.78 ± 0.05	0.62 ± 0.10	320.8	56.4	6

Notes. All temperatures are given in the main-beam temperature scale. [(a)] Fixed to compute the upper limit in the line area.

antennas in the D configuration and six antennas in the C configuration. The baseline lengths ranged between 24 and 176 m. We observed a 19-field mosaic in a hexagonal pattern covering an almost circular field-of-view of 80″ in diameter. The observations used about 19 h of telescope time. The on-source time scaled to a six antenna array is 5.3 h after filtering out low-quality visibilities. Two correlator windows of 20 MHz (yielding a spectral resolution of 39 kHz) were concatenated to cover both CH_3OH lines. Another 20 MHz window was centered on the targeted H_2CO line. During the observations, the typical precipitable water vapor amounted to 6 mm and the typical system temperature was 145 K. The median noise level achieved over the mosaic is 0.24 K and 0.12 K (T_{mb}, in channels of 0.2 km s^{-1} width) for H_2CO and CH_3OH, respectively.

We used the standard algorithms implemented in the GILDAS[1]/CLIC software to calibrate the PdBI data. The radio-frequency bandpass was calibrated by observing the bright quasar 3C 454.3. Phase and amplitude temporal variations where calibrated by fitting spline polynomials through regular mesurements of two nearby quasars (0420−014 and 0528+134). The PdBI secondary flux calibrator MWC 349 was observed once

[1] See http://www.iram.fr/IRAMFR/GILDAS for more information about the GILDAS softwares (Pety 2005).

during every track, which allowed us to derive the flux scale of the interferometric data. The absolute flux accuracy is ∼10%.

2.2. 30 m maps

A multiplicative interferometer filters out the low spatial frequencies, that is, spatially extended emission. We therefore observed the same region with the IRAM-30 m single-dish telescope to recover the low spatial frequency (short- and zero-spacing) information filtered out by the PdBI. The H_2CO $2_{02}-1_{01}$ (145.603 GHz) line was observed simultaneously with the CH_3OH-E $3_{-1}-2_{-1}$ (145.097 GHz) and CH_3OH-A 3_0-2_0 (145.103 GHz) lines during ∼13 h of average summer weather in August and September 2012. We used the two polarizations of the EMIR receivers and the FTS backends at 49 kHz spectral resolution. We used the position-switching, on-the-fly observing mode. The off-position offsets were $(\delta RA, \delta Dec) = (100'', 0'')$, that is, the H II region ionized by σOri and free of molecular emission. We completed the observations of the 146.097 GHz and 146.103 GHz CH_3OH lines with older but higher-quality observations obtained in January 2007. We used one polarization of the C150 receiver and one 20 MHz window of the VESPA correlator, yielding a spectral resolution of 20 kHz. In this case, we used the frequency-switched, on-the-fly observing mode, with a frequency throw of 7.9 MHz. In both observations, we observed along and perpendicular to the direction of the exciting star in zigzags (i.e., ± the lambda and beta scanning direction). From our knowledge of the IRAM-30 m telescope, we estimate the absolute position accuracy to be 3″.

The IRAM-30 m data were processed with the GILDAS/CLASS software. The data were first calibrated to the T_A^* scale using the chopper-wheel method (Penzias & Burrus 1973). The mixer tuning tables were incorrect for the frequency tuned in 2012. This basically turned the single sideband mixers into double-sideband ones. Because the actual rejection was unknown, we were unable to recompute an accurate T_A^* scale. Instead, we fixed the 2012 T_A^* scale according to the 2007 scale, which was correct. To do this, we correlated the 2007 and 2012 CH_3OH data sets, which allowed us to determine the multiplicative factors needed to fix the 2012 data (1.9 and 2.4 for the vertical and horizontal polarizations, respectively). We applied the same factors for the H_2CO data that were acquired with the same tuning. The data were converted to main-beam temperatures (T_{mb}) using the forward and main-beam efficiencies (F_{eff} and B_{eff}). The resulting amplitude accuracy is 10%. We then computed the experimental noise by subtracting a zeroth-order baseline from every spectra. A systematic comparison of this noise value with the theoretical noise computed from the system temperature, the integration time, and the channel width allowed us to filter out outlier spectra. The spectra where then gridded to a data cube through a convolution with a Gaussian kernel. Finally, we fitted another baseline of order 3 through each spectra of the cube.

2.3. Joint imaging and deconvolving of the interferometric and single-dish data

Following Rodriguez-Fernandez et al. (2008), the GILDAS/MAPPING software and the single-dish map from the IRAM-30 m were used to create the short-spacing visibilities not sampled by the Plateau de Bure interferometer. In short, the maps were deconvolved from the IRAM-30 m beam in the Fourier plane before multiplication by the PdBI primary beam in the image plane. After a last Fourier transform, pseudo-visibilities were sampled between 0 and 15 m (the diameter of the PdBI antenna). These visibilities were then merged with the interferometric observations. Each mosaic field was imaged and a dirty mosaic was built by combining these fields in the following best way in terms of signal-to-noise ratio (Pety & Rodríguez-Fernández 2010). The resulting data cubes were then scaled from Jy/beam to T_{mb} temperature scale using the synthesized beam size (see Table 2).

2.4. Deep pointed integrations with the 30 m

These observations are part of the Horsehead WHISPER project (Wideband High-resolution Iram-30 m Surveys at two Positions with Emir Receivers, PI: J. Pety), a complete and unbiased line survey at 1, 2, and 3 mm, carried out with the IRAM-30 m telescope. Two positions were observed: 1) the HCO peak, which is characteristic of the photo-dissociation region at the surface of the Horsehead nebula (Gerin et al. 2009); and 2) the DCO^+ peak, which belongs to a cold condensation located less than 40″ away from the PDR edge, where HCO^+ and other species are highly deuterated (Pety et al. 2007). Hereafter we refer to these two positions as the PDR and dense core, respectively. The combination of the new EMIR receivers at the IRAM-30 m telescope and the Fourier transform spectrometers (FTS) yields a spectral survey with unprecedented combination of bandwidth (36 GHz at 3 mm, 25 GHz at 2 mm and 76 GHz at 1 mm), spectral resolution (49 kHz at 3 and 2 mm; and 195 kHz at 1 mm), and sensitivity (median noise 8.1 mK, 18.5 mK and 8.3 mK, respectively). A detailed presentation of the observing strategy and data reduction process will be given in a forthcoming paper. In short, all frequencies were observed with two different frequency tunings and the Horsehead PDR and dense-core positions were alternatively observed every 15 min in position-switching mode with a common fixed off-position. This observing strategy allows us to remove potential ghost lines that are incompletely rejected from a strong line in the image sideband (the typical rejection of the EMIR sideband-separating mixers is only 13dB).

2.5. Deep pointed integrations with the CSO

We also report the detection of a new H_2CO line in the Horsehead. The H_2CO $4_{13}-3_{12}$ at line at 300.836 GHz was observed at the Caltech Submillimeter Observatory (CSO) telescope in October 2012. We used the Barney receiver and the FFTS2 backends at 269 kHz spectral resolution. We used the position-switching mode with the same off-position as was used in the 30 m observations, that is, $(\delta RA, \delta Dec) = (100'', 0'')$. The data were processed with the GILDAS/CLASS software. A fourth-order baseline was fit and subtracted from the spectra. The data were converted to T_{mb} using a beam efficiency of 0.68 measured towards Jupiter.

3. Observational results

3.1. Deep pointed integrations

Figure 1 presents the CH_3OH lines detected in the Horsehead. A diagram with the lower-energy rotational levels of E- and A-type methanol is shown in Fig. 2, with color arrows indicating the detected lines. We detected 9 and 16 lines at the PDR and dense-core positions, respectively. Of these lines, at each position, three arise from A-type methanol and the rest arise from E-type methanol. The brightest CH_3OH lines are those arising from A-type symmetry species. All lines are brighter in

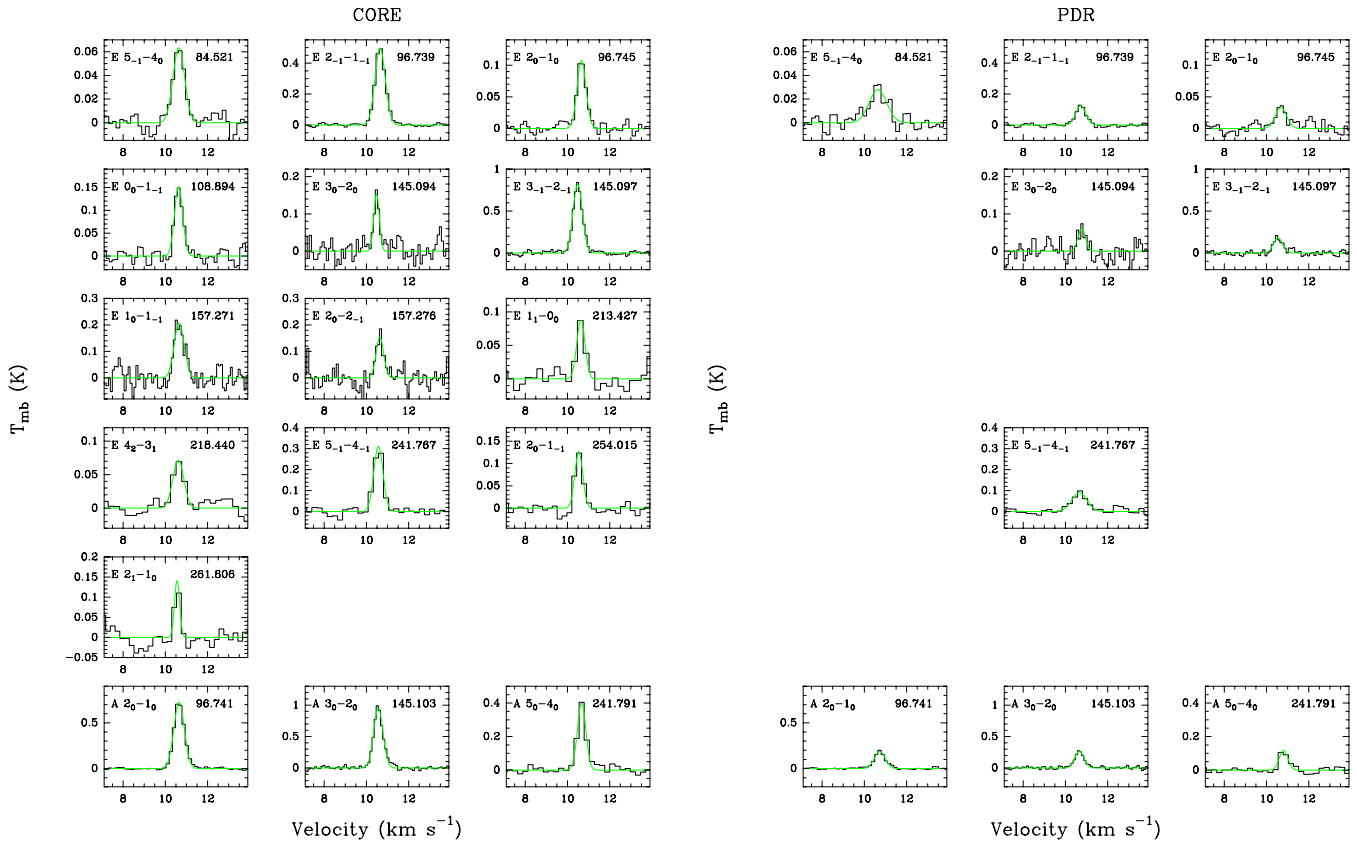

Fig. 1. Detected CH_3OH lines toward the dense-core (*left*) and PDR (*right*) positions. The green curves are Gaussian fits. The line frequency in GHz is given in each box. For each line, the same scale is used at both positions to facilitate the comparison.

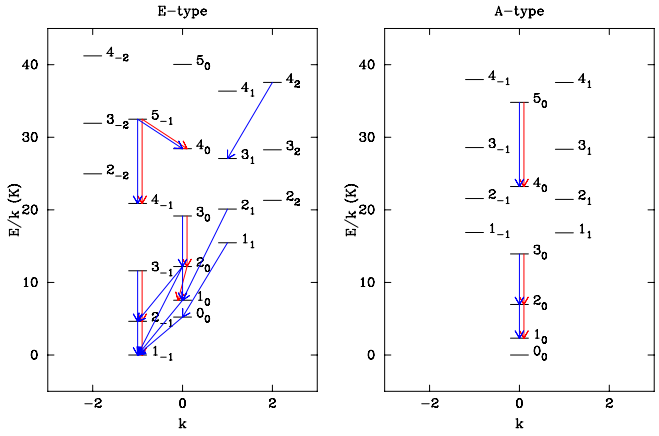

Fig. 2. Lower-energy rotational levels of CH_3OH – E (*left*) and CH_3OH – A (*right*). The arrows indicate the lines detected in the PDR (red) and the core (blue).

the dense core than in the PDR. The same behavior was found for H_2CO (Guzmán et al. 2011). Gaussian fits of the CH_3OH lines at the PDR in general result in broader line widths than at the dense core, although a few lines have similar linewidths toward both positions.

3.2. 30m maps

Figure 3 displays the single-dish maps of the 1.2 mm dust continuum emission and the line-integrated emission of the $DCO^+(3-2)$ (216 GHz) line, the p – H_2CO 3_{03}–2_{02} (218 GHz) and 2_{02}–1_{01} (146 GHz) lines, the CH_3OH – E 3_{-1}–2_{-1} (146 GHz) line, and the CH_3OH – A 3_0–2_0 (146 GHz) line. The formaldehyde and methanol emission to first order resembles the dust continuum spatial distribution. It first follows the photo-dissociation front, that is, the top of the Horsehead nebula from its front to its mane. It then forms two filaments almost perpendicular to the photo-dissociation front, one of them delineating the Horsehead throat. The E- and A-type methanol emission shows similar spatial distributions.

In contrast to the DCO^+ emission, which delineates a narrow filament, formaldehyde and methanol emission is extended. The impression that the formaldehyde emission is slightly more extended than the methanol emission is an artifact related to the different signal-to-noise ratio of these maps. Indeed, the 146 GHz E-type methanol map has by far the lowest signal-to-noise ratio. The highest signal-to-noise ratio map (i.e., the 146 GHz formaldehyde one) thus indicates that both formaldehyde and methanol emit in the PDR region (green cross).

Although the methanol emission in general correlates well with the formaldehyde emission, there are a few differences. First, formaldehyde peaks on the right side (closest to the photo-dissociation front) of the dense core as traced by the DCO^+ emission, while methanol peaks on its left side. Second, the 146 GHz formaldehyde line peaks at the DCO^+ emission peak (blue cross), where the gas is cold ($T_{kin} \simeq 20$ K) and dense ($n_H \sim 10^5$ cm^{-3}), while CH_3OH presents a local minimum at the same position.

3.3. PdBI maps

Figure 4 displays the HCO $1_{01}3/2,2$–$0_{00}1/2,1$ (86.670 GHz), H_2CO 2_{02}–1_{01} (145.602 GHz), CH_3OH – E 3_{-1}–2_{-1} (145.097 GHz), and CH_3OH – A 3_0–2_0 (145.103 GHz) integrated intensity maps obtained with the PdBI. In contrast

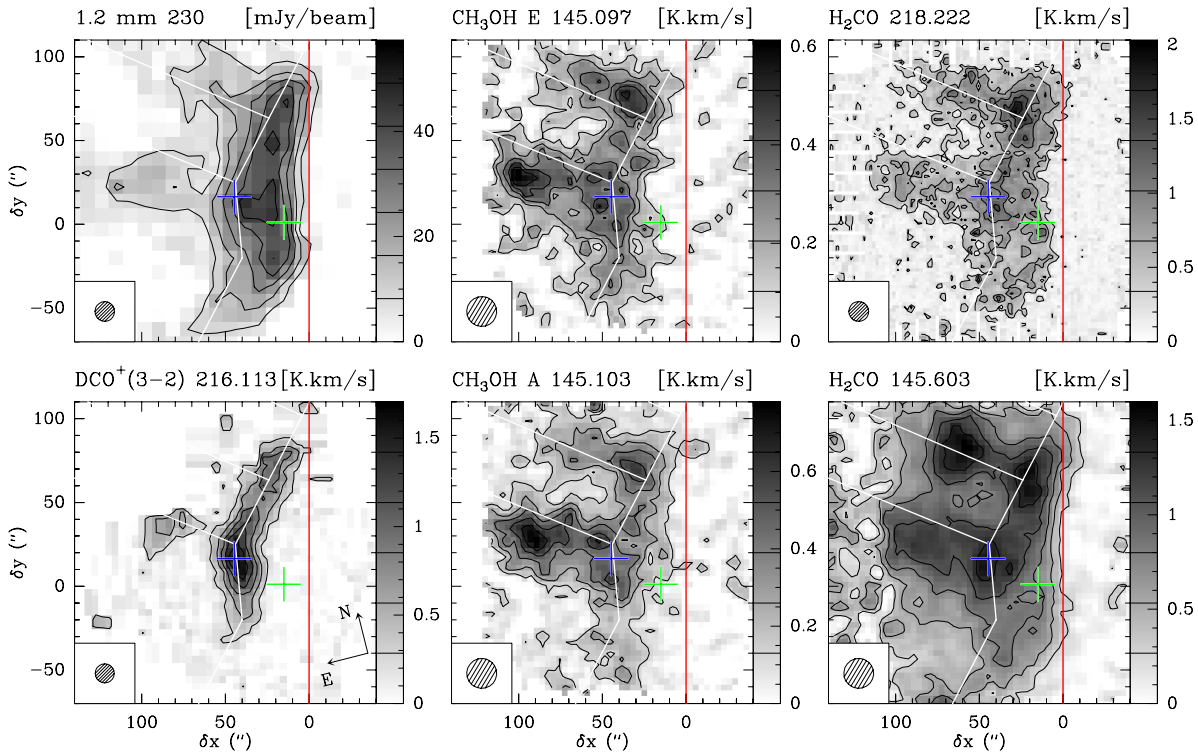

Fig. 3. IRAM-30 m maps of the Horsehead edge. Maps were rotated by 14° counterclockwise around the projection center, located at $(\delta x, \delta y) = (20'', 0'')$, to bring the exciting star direction in the horizontal direction, and the horizontal zero was set at the PDR edge, delineated by the red vertical line. The crosses show the positions of the PDR (green) and the dense core (blue), where deep integrations were performed at IRAM-30 m. The white lines delineate the arc-like structure of the DCO^+ emission. The spatial resolution is plotted in the bottom-left corner. Values of contour levels are shown in the respective image lookup table. The emission of all lines is integrated between 10.1 and 11.1 km s^{-1}.

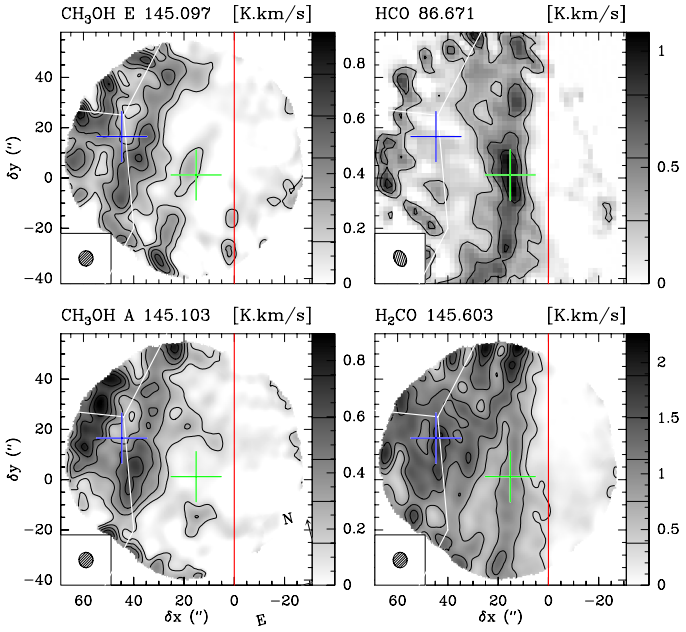

Fig. 4. IRAM-PdBI maps of the Horsehead edge. The field of view is smaller than in Fig. 3. The angular resolution is 6.″7 × 4.″4 for HCO and 6.″1×5.″6 for H_2CO and CH_3OH. All other descriptions are identical to Fig. 3.

to the case of HCO, which peaks in the PDR, the H_2CO and CH_3OH lines are brighter in the more UV-shielded layers of the nebula. However, the filament traced by the HCO emission is clearly seen in the H_2CO map at the PDR edge. The exact spatial distribution of the CH_3OH emission near the PDR position is difficult to infer due to the low signal-to-noise ratio at this position.

The minimum seen in the methanol 30 m maps near the dense-core position (blue cross) is present in both methanol lines and is preserved in the higher angular resolution map. On the other hand, H_2CO, which was observed simultaneously with CH_3OH, peaks at the dense core. This suggests that 1) the methanol gap is real and not an artifact of the deconvolution; and 2) methanol and formaldehyde emission show opposite behavior at the DCO^+ peak.

In contrast with HCO data, the maps of H_2CO and CH_3OH emission obtained with the PdBI only data (i.e., without the short-spacings from the IRAM-30 m telescope) looks like noise with a typical noise level of 0.15 K. Indeed, the spectra extracted from the hybrid synthesis (PdBI + 30 m) cube at the position of the dense core and of the PDR have an integrated area compatible, within the noise level, with the 30 m spectra at the same positions. This implies that the beam dilution of the single-dish observations of H_2CO and CH_3OH is marginal. We therefore used the higher signal-to-noise ratio 30 m spectra to infer the column densities at the PDR and dense-core positions.

4. Column densities and abundances

4.1. H_2CO

Figure 5 shows the new o-H_2CO $4_{13}-3_{12}$ line detected in the Horsehead. Guzmán et al. (2011) reported the detection of four o-H_2CO lines at lower frequencies. They used a nonlocal excitation and radiative transfer model from Goicoechea et al. (2006) adapted to the Horsehead geometry to model the observed H_2CO line intensities. The parameters they used are $T_{\rm kin}$ = 60 K and $n(H_2) = 6 \times 10^4$ cm^{-3} at the PDR position

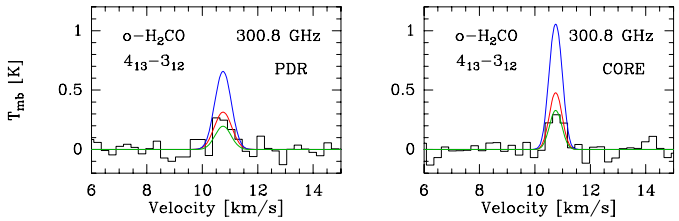

Fig. 5. New o-H_2CO line detected toward the PDR (*left*) and dense-core (*right*) positions. The three color lines plot the radiative-transfer models from Guzmán et al. (2011), where the column density was varied around the best match (red curve) by a factor of 1.5 (blue curve) and 1/1.5 (green curve). The column density used for the best fit is given in Table 6. The line frequency in GHz is given in each box.

Table 4. Critical densities[a] (cm^{-3}) for the CH_3OH lines detected in this work with p-H_2 and o-H_2 as colliding partners computed for two kinetic temperatures.

		T_{kin} = 20 K		T_{kin} = 60 K	
Type	J_K	p-H_2	o-H_2	p-H_2	o-H_2
E	5_{-1}	2.47×10^5	1.91×10^5	2.52×10^5	2.08×10^5
	2_{-1}	2.81×10^4	2.33×10^4	2.66×10^4	2.33×10^4
	2_0	3.28×10^5	1.52×10^5	3.59×10^5	1.55×10^5
	0_0	–	1.58×10^5	–	2.16×10^5
	3_0	4.13×10^5	2.88×10^5	4.40×10^5	2.83×10^5
	3_{-1}	7.05×10^4	6.88×10^4	6.88×10^4	6.83×10^4
	1_0	3.73×10^5	1.11×10^5	3.75×10^5	1.14×10^5
	1_1	2.70×10^6	2.62×10^5	3.83×10^6	2.83×10^5
	4_2	3.58×10^5	1.87×10^5	3.50×10^5	1.94×10^5
	2_1	6.75×10^5	2.88×10^5	7.19×10^5	2.83×10^5
A	5_{-1}	2.28×10^5	2.06×10^5	2.45×10^5	2.20×10^5
	2_{-1}	6.70×10^4	6.56×10^4	7.04×10^4	7.35×10^4
	2_0	2.86×10^4	2.29×10^4	2.96×10^4	2.58×10^4

Notes. [a] Computed as $n_{cr}(J'_{K'_aK'_c}, T_{kin}) = \frac{\sum_{J''_{K''_aK''_c}} A(J'_{K'_aK'_c}\rightarrow J''_{K''_aK''_c})}{\sum_{J''_{K''_aK''_c}} \gamma(J'_{K'_aK'_c}\rightarrow J''_{K''_aK''_c}, T_{kin})}$.

and T_{kin} = 20 K and $n(H_2) = 10^5$ cm^{-3} at the dense-core position. The column density that best reproduced the observations is given in Table 6 and the modeled line profile is shown in red in Fig. 5. The line profiles for two other models are also shown. The new detected H_2CO line agrees with the predictions of our previous model and thus corroborates the H_2CO column density derived by Guzmán et al. (2011).

4.2. CH_3OH

Typical densities in the Horsehead ($n_H = 10^4$–10^5 cm^{-3}) are lower than the critical densities of the observed transitions of methanol (see Table 4). We therefore expect the lines to be subthermally excited ($T_{ex} \ll T_{kin}$), and a non-LTE approach is needed to compute the CH_3OH column densities. E and A symmetries of CH_3OH were treated as different species because radiative transitions between them occur on timescales too long compared with the lifetime of the molecules. We did not correct for beam-dilution factors because the interferometric maps indicate that beam dilution is marginal for these molecules. The spectroscopic parameters for the detected transitions are given in Table 5.

We performed non-LTE radiative-transfer modeling using the RADEX LVG model (van der Tak et al. 2007), which computes the line intensities of a species for a given column density, kinetic temperature, and density of H_2. We included 100 rotational levels for CH_3OH – E and CH_3OH – A, where the highest energy level lies at ∼155 cm^{-1} for both species. We considered p-H_2 and o-H_2 as collision partners with collisional excitation rates from Rabli & Flower (2010). An H_2 ortho-to-para ratio of 3 (high-temperature limit) was assumed in the models. Lower H_2 ortho-to-para ratios were also tested, and we found that the difference is negligible. We also investigated the importance of electrons in the excitation at the PDR. The electron fraction is 10^{-4} relative to H_2 in the PDR position, while in the dense core the electron fraction is $\sim10^{-9}$ (Goicoechea et al. 2009b). We computed the CH_3OH – E–electron and CH_3OH – A–electron collisional coefficients within the dipolar Born approximation (e.g., Itikawa 1971). Owing to the relatively large dipole of methanol (1.7 D), dipole-allowed cross sections are expected to be dominant and mostly determined by the long-range electron-dipole interaction. Thus, for the water molecule, which has a similar dipole (1.8 D), Faure et al. (2004) have shown that the Born approximation is accurate down to typically 1 eV. At lower energy, short-range forces can become important, and these effects were found to reduce the low-energy cross-sections by up to a factor of ∼1.5. In the case of methanol, the Born treatment probably overestimates the rotational cross-sections by a factor of 2–3, as suggested by the measurements of the total elastic cross-section (see Vinodkumar et al. 2013, and references therein). In the Born approximation, cross-sections are proportional to line strengths and the square of the dipole and therefore strictly obey the dipolar selection rule. In this work, line strengths and dipoles were taken from the JPL catalog (Pickett et al. 1998). Excitation cross-sections were computed in the energy range 0.1 meV–1 eV and rate coefficients were deduced in the range 10–1000 K, for the lowest 256 levels of CH_3OH – A (1853 transitions) and the lowest 256 levels of CH_3OH – E (2324 transitions).

We first constrained the column density of CH_3OH – E because we detected more lines of this species. The density profile across the PDR in the Horsehead is well constrained (Habart et al. 2005). Several efforts have been made to compute the thermal profile, but it remains less well constrained than the density. We therefore decided to fix the H_2 density and vary the temperature in our models. For this, we ran grids of models for kinetic

Table 5. Spectroscopic parameters of the detected lines obtained from the CDMS data base (Müller et al. 2001).

Molecule	Transition	ν [GHz]	E_u [K]	A_{ul} [s^{-1}]	g_u
CH_3OH – E	5_{-1}–4_0	84.521	40.4	2.0×10^{-6}	11
CH_3OH – E	2_{-1}–1_{-1}	96.739	12.5	3.0×10^{-6}	5
CH_3OH – E	2_0–1_0	96.745	20.1	3.0×10^{-6}	5
CH_3OH – E	0_0–1_{-1}	108.894	13.1	1.5×10^{-5}	1
CH_3OH – E	3_0–2_0	145.094	27.1	1.2×10^{-5}	7
CH_3OH – E	3_{-1}–2_{-1}	145.097	19.5	1.1×10^{-5}	7
CH_3OH – E	1_0–1_{-1}	157.271	15.4	2.2×10^{-5}	3
CH_3OH – E	2_0–2_{-1}	157.276	20.1	2.2×10^{-5}	5
CH_3OH – E	1_1–0_0	213.427	23.4	3.4×10^{-5}	3
CH_3OH – E	4_2–3_1	218.440	45.5	4.7×10^{-5}	9
CH_3OH – E	5_{-1}–4_{-1}	241.767	40.4	5.8×10^{-5}	11
CH_3OH – E	2_0–1_{-1}	254.015	20.1	1.9×10^{-5}	5
CH_3OH – E	2_1–1_0	261.806	28.0	5.6×10^{-5}	5
CH_3OH – A	2_0–1_0	96.741	7.0	3.0×10^{-6}	5
CH_3OH – A	3_0–2_0	145.103	13.9	1.2×10^{-5}	7
CH_3OH – A	5_0–4_0	241.791	34.8	6.0×10^{-5}	11

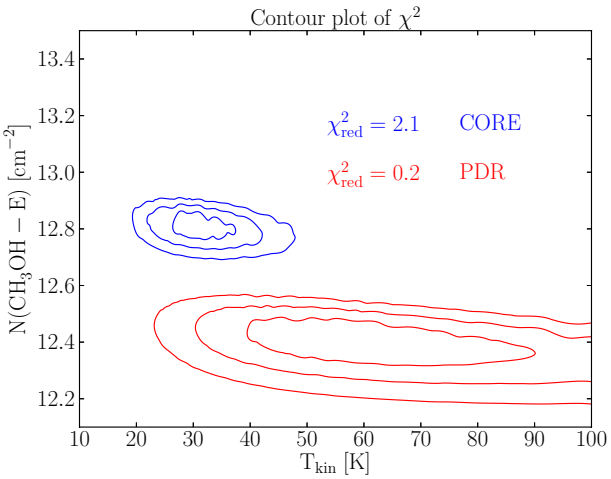

Fig. 6. χ^2 as a function of N(CH_3OH – E) and T_{kin} for the PDR (red) and dense-core (blue) positions. The H_2 density was kept constant to $n(H_2) = 6 \times 10^4$ cm^{-3} (PDR) and $n(H_2) = 1 \times 10^5$ cm^{-3} (dense core). The contours indicate the 1, 2, and 3σ confidence levels for the models. The reduced χ^2, defined as $\chi^2_{red} = \chi^2/(N-2)$, is shown for the best-fit model at each position.

temperatures of 10–100 K and CH_3OH – E column densities between 10^{11} and 10^{15} cm^{-2}. The density of H_2 was kept constant to the well-known values of $n_H = 6 \times 10^4$ cm^{-3} in the PDR and $n_H = 1 \times 10^5$ cm^{-3} in the dense core. Then, the χ^2 was computed[2] at each point of the grid to determine the best-fit parameters. Figure 6 shows the 1, 2, and 3σ confidence levels for the PDR (red) and dense core (blue) for models without electron excitation. The best fits are for kinetic temperatures of 60 K (PDR) and 30 K (core), which agrees well with previous determinations. The CH_3OH – E column densities are well constrained. The best fits are for CH_3OH – E column densities of $(2.7 \pm 0.5) \times 10^{12}$ cm^{-2} and $(6.5 \pm 0.8) \times 10^{12}$ cm^{-2} for the PDR and dense core, respectively. We also ran models for a fixed kinetic temperature instead of a fixed gas density. These models resulted in similar CH_3OH column densities, but in a H_2 gas density of $n_H = 6 \times 10^4$ cm^{-3} at the dense-core position, which is lower than expected ($n_H \sim 10^5$ cm^{-3}).

We found that the change in the CH_3OH – E column density is negligible in these models when we included the electron excitation. However, for a grid of models with the three parameters (T_{kin}, n_H and $N(CH_3OH)$) free and no electron excitation, we found a low kinetic temperature ($T_{kin} = 40$ K) and a high density ($n_H = 10^5$) at the PDR. When we included the electron excitation, on the other hand, we obtained $T_{kin} \sim 65$ K and $n_H \sim 5 \times 10^4$ cm^{-3}, which agrees much better with previous estimates. The inferred CH_3OH column density is the same for both models ($N = 2.7 \times 10^{12}$ cm^{-2}). Hence, collisions with electrons are not important for determining the CH_3OH column density, but they are important for determining the kinetic temperature and density of the gas. The electron excitation was found to be important for determining the column density of CH_3CN in the PDR (Gratier et al. 2013).

The determination of the CH_3OH – A column density is more difficult because only three lines were detected, which provides fewer constrains to the model. We therefore fixed the kinetic temperature to the best-fit values found for CH_3OH – E, in addition to keeping the density of H_2 constant, and ran models varying the column density only. The best fits are obtained for CH_3OH – A column densities of $(2.0 \pm 0.3) \times 10^{12}$ cm^{-2} and $(8.1 \pm 1.0) \times 10^{12}$ cm^{-2} for the PDR and dense core, respectively.

[2] $\chi^2 = \sum_1^N \frac{(\text{Observation} - \text{Model})^2}{\sigma^2}$, with N the number of detected lines.

Table 6. Column densities and abundances.

	Molecule	PDR	Dense core
Column density [cm^{-2}]	N_H	3.8×10^{22}	6.4×10^{22}
	N(HCO)[a]	3.2×10^{13}	$<4.6 \times 10^{12}$
	N(o-H_2CO)[b]	7.2×10^{12}	9.6×10^{12}
	N(p – H_2CO)[b]	3.6×10^{12}	3.2×10^{12}
	N(CH_3OH – E)	2.7×10^{12}	6.5×10^{12}
	N(CH_3OH – A)	2.0×10^{12}	8.1×10^{12}
Abundances $\frac{N(X)}{(N(H)+2\,N(H_2))}$	[HCO]	8.4×10^{-10}	$<7.2 \times 10^{-11}$
	[o-H_2CO]	1.9×10^{-10}	1.5×10^{-10}
	[p – H_2CO]	9.5×10^{-11}	5.0×10^{-11}
	[CH_3OH – E]	7.0×10^{-11}	1.0×10^{-10}
	[CH_3OH – A]	5.3×10^{-11}	1.3×10^{-10}
	H_2CO/CH_3OH[c]	2.3 ± 0.4	0.9 ± 0.1

Notes. [(a)] Gerin et al. (2009). [(b)] Guzmán et al. (2011). [(c)] We estimated an error of ~15% for the H_2CO column density (similar to CH_3OH) in computing the error in the ratio.

Table 6 summarizes the derived column densities and abundances relative to the total number of atomic hydrogen atoms for HCO, H_2CO, and CH_3OH. The E/A methanol ratio is 1.3 ± 0.3 and 0.8 ± 0.1 for the PDR and dense core, respectively. The total CH_3OH abundance is similar in the PDR and dense core, being only a factor ~ 1.9 larger in the dense core. Similar abundances were also found for H_2CO in both positions. The H_2CO/CH_3OH abundance ratio is $\sim 2.3 \pm 0.4$ in the PDR and $\sim 0.9 \pm 0.1$ in the dense core.

4.3. Deuterated CH_3OH

Guzmán et al. (2011) detected single and doubly deuterated formaldehyde in the Horsehead and derived [HDCO]/[H_2CO] = 0.11 and [D_2CO]/[H_2CO] = 0.04 in the dense core. We now searched for deuterated methanol at this position. We did not detect transitions from deuterated methanol, but we computed an upper limit for the CH_2DOH column density toward the dense core. The low-energy transitions $2_K - 2_K$ of CH_2DOH lie at 89 GHz. The rms noise at this frequency is 6.43 mK with 0.17 km s^{-1} spectral resolution. Assuming a linewidth of 0.5 km s^{-1}, we obtain an upper limit for the integrated line intensity of 6 mK km s^{-1}. This translates into a 1σ upper limit for the column density of 1.4×10^{12} cm^{-2} and a fractionation ratio [CH_2DOH/CH_3OH] $\leq$ 0.26 at the dense-core position. Assuming that methanol has fractionation levels similar to those of H_2CO, we conclude that our data are not sensitive enough to detect lines from deuterated methanol molecules. For reference, singly, doubly, and even triply deuterated methanol species such as CH_2DOH, CHD_2OH, and CD_3OH have been detected toward low-mass protostars with abundance ratios of 37–65% (CH_2DOH), 20% (CHD_2OH), and 1.4% (CD_3OH) compared to their non-deuterated isotopologue (Parise et al. 2004, 2006).

5. Comparison with models

In this section we study the HCO, H_2CO, and CH_3OH chemistry in the Horsehead. We used an updated version of the one-dimensional, steady-state photochemical model (Le Petit et al. 2006) used in the study of H_2CO by Guzmán et al. (2011). We

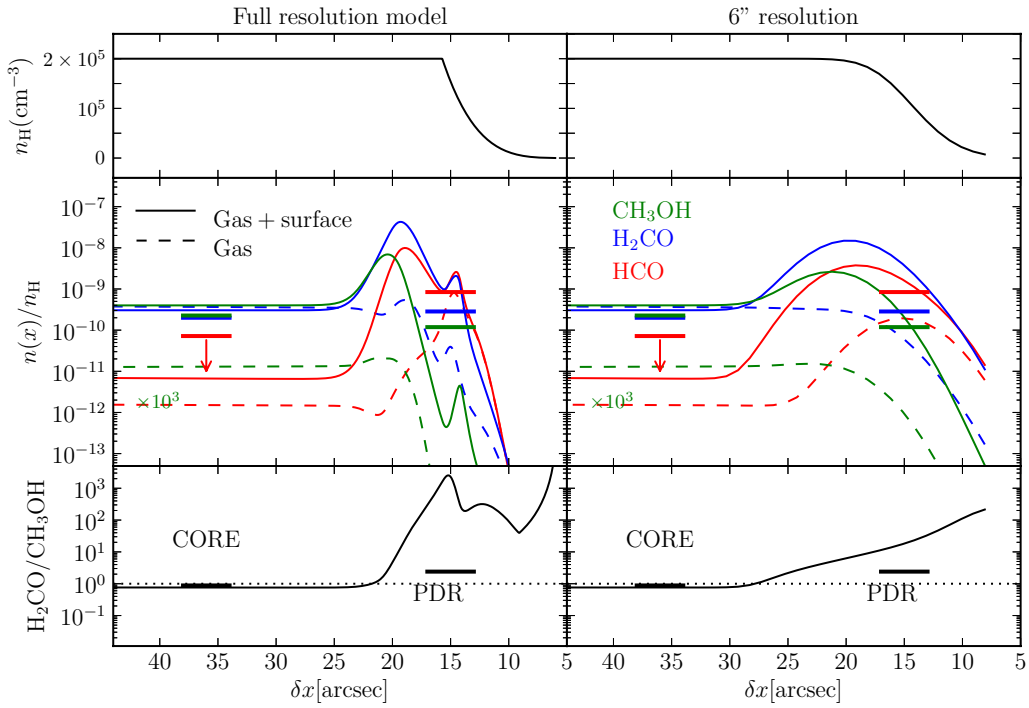

Fig. 7. Photochemical model of the Horsehead PDR. The *left column* shows the full-resolution model and the *right column* shows the model convolved with a Gaussian of 6″ FWHM. *Upper panel*: PDR density profile ($n_H = n(H) + 2n(H_2)$ in cm^{-3}). *Middle panel*: predicted abundance (relative to n_H) of HCO (red), H_2CO (blue) and CH_3OH (green). *Lower panel*: predicted H_2CO/CH_3OH abundance ratio. Models shown as dashed lines include pure gas-phase chemistry and models shown as solid lines include both gas-phase and grain surface chemistry. The CH_3OH abundance predicted by the pure gas-phase model has been multiplied by 10^3 in the *middle panel* so that it could fit in the figure.

include the density profile displayed in the upper panel of Fig. 7, a radiation field $\chi = 60$ (relative to the Draine field; Draine 1978), the elemental gas-phase abundances from Goicoechea et al. (2009b; see their Table 5), and a cosmic-ray ionization rate $\zeta = 5 \times 10^{-17}$ s^{-1} per H_2 molecule.

We compare the results of a pure gas-phase chemical network with one that also includes grain surface reactions. Figure 7 displays the results for the photochemical models. The left column presents the results computed by the code, which samples the UV-illuminated gas on a finer spatial grid than the UV-shielded gas to correctly represent the steep physical and chemical gradients. The right column presents the results convolved with a Gaussian of 6″ (FWHM) to facilitate the comparison with the abundances inferred from the PdBI observations at 6″ angular resolution. The predicted H_2CO and CH_3OH abundance profiles are shown in the middle panel. The H_2CO/CH_3OH abundance ratio is shown in the lower panel. The horizontal bars show the results inferred from observations. Results for the pure gas-phase model are shown as dashed lines and results for the model including grain surface chemistry are shown as solid lines.

5.1. Pure gas-phase models

We used a modified version of the pure gas-phase chemical network of the Ohio State University (OSU). Our network includes the photodissociation of HCO and of H_2CO (leading to CO and H_2), and the atomic oxygen reaction with the methylene radical (CH_2) to explain the high abundance of HCO in the PDR (Gerin et al. 2009). The H_2CO photodissociation channel that leads to HCO + H is also included.

As previously shown by Guzmán et al. (2011), the pure-gas phase model satisfactorily reproduces the observed H_2CO abundance in the dense core ($\delta x \sim 35''$), but it underestimates the abundance in the PDR ($\delta x \sim 15''$) by at least one order of magnitude. In this model the formation of H_2CO is dominated by reactions between oxygen atoms and the methyl radical (CH_3) in both the PDR and dense core. The destruction of H_2CO in the PDR is dominated by reactions with S^+ and by photodissociation, while it is dominated by reactions with ions (mainly H_3O^+, HCO^+ and S^+) in the dense core.

In the gas phase, methanol is mainly produced by the dissociative recombination of $CH_3OH_2^+$, which is formed by reactions between CH_3^+ and water. It is now well established that this reaction is not efficient enough to explain the observed CH_3OH abundances (Garrod et al. 2006; Geppert et al. 2006). Indeed, the pure gas-phase model underestimates the CH_3OH abundance by ∼5 orders of magnitude in both the PDR and dense core. Note that the CH_3OH abundance predicted by the pure gas-phase model has been multiplied by 1000 in Fig. 7.

5.2. Grain surface chemistry models

We included the reactions on the surface of dust grains to the gas-phase chemical network described in Sect. 5.1. A detailed description of the implementation of grain surface chemistry in the Meudon PDR code will be given in a subsequent paper (Le Bourlot et al., in prep.). The model includes the adsorption, desorption, and diffusive reactions on grains, where the sequence to form formaldehyde and methanol is the one shown in the hydrogenation path (1). We also introduce water formation via hydrogenation reactions of O, OH until H_2O. The hydrogenation of formaldehyde can lead to CH_3O and/or CH_2OH. Gas-phase methoxy radical (CH_3O) was recently detected in the cold dense core B1-b (Cernicharo et al. 2012). We do not distinguish between these two isomers, that is, CH_3O and CH_2OH, in our network. The energy barriers associated with the H + CO (200 K)

and $H + H_2CO$ (300 K) reactions have been modified with respect to Guzmán et al. (2011). As shown by laboratory studies (Öberg et al. 2009b,a; Muñoz Caro et al. 2010), photodesorption can be an efficient mechanism to release molecules into the gas phase in regions exposed to radiation fields. We included photodesorption yields of 10^{-3} and 2×10^{-4} molecules per incident UV photon, for H_2CO and CH_3OH, respectively. These values are close to those measured in the laboratory for CO, CO_2, H_2O, and CH_3OH (Öberg et al. 2007, 2009a–c). Photodesorption of adsorbed CH_3OH can produce both methanol and formaldehyde in the gas-phase with a 50/50 branching ratio. This channel was not included in the model of Guzmán et al. (2011), where photodesorption of adsorbed CH_3OH produced only gas-phase methanol. We checked that the use of steady-state chemistry in the model is a valid assumption for the physical conditions prevailing in the Horsehead PDR and dense core. Indeed, the formation and destruction timescales of H_2CO and CH_3OH are <30 yr and <5000 yr at the PDR and dense core, respectively, while the estimated age of the Horsehead is $\sim 5 \times 10^5$ yr (Pound et al. 2003).

The new results are shown as solid lines in Fig. 7. The dust temperatures in this model are 20 K. The model predicts two abundance peaks at the edge of the nebula ($\delta x \sim 15$ and $\delta x \sim 20$), with CH_3OH peaking deeper inside the cloud than HCO and H_2CO, and an abundance plateau at the inner layers of the cloud. This way, HCO and H_2CO dominate at the outer layers of the cloud, while CH_3OH dominates in the inner layers. At the dense-core position ($\delta x \sim 35''$), the modeled H_2CO abundance is similar to the one predicted by the pure gas-phase model. The CH_3OH abundance, on the other hand, increases by ~5 orders of magnitude with respect to the pure gas-phase model. The observed H_2CO and CH_3OH abundances in the dense core are well reproduced by the model that includes both gas-phase and grain surface chemistry. In the PDR, this model also agrees well with the observed HCO and CH_3OH abundances, but the predicted H_2CO abundance is higher than observed.

In this model, CH_3OH is produced by photodesorption of CH_3OH ices everywhere in the cloud. At the dense core, the FUV photons that photodesorb the CH_3OH ices are secondary photons produced by the interaction between cosmic rays and H_2 molecules. Gas-phase CH_3OH is mainly destroyed by photodissociation in the PDR and by freeze-out in the dense core. H_2CO is produced mainly by direct photodesorption of H_2CO ices in the PDR position. In the model of Guzmán et al. (2011), we found that the dominant formation path for H_2CO in the dense core was the gas-phase route that involved CH_3 and O. With this new model, we find that at the dense core H_2CO is produced mainly by photodissociation of CH_3OH ices. This difference is the result of the several modifications made to the model, of which the most important is the inclusion of the channel that leads to H_2CO in the photodesorption of CH_3OH ice. H_2CO is mainly destroyed by photodissociation in the PDR and by reactions with ions (mainly N_2H^+ and H_3^+) in the dense core[3].

[3] We first ran models assuming the solar sulfur abundance (S/H = 1.38×10^{-5}). With this S abundance and including the grain surface chemistry, the destruction of H_2CO is dominated by reactions with S^+ in both the PDR and dense core. We then ran models using a lower sulfur abundance (S/H = 3.5×10^{-6}), which reproduces the observed CS and HCS^+ abundances (Goicoechea et al. 2006). In this model, which is the one adopted in this paper, S^+ is not important in the destruction of H_2CO. As a result, the predicted H_2CO abundance at the dense core is three times higher in the low-S abundance model and the agreement between model and observations is better. We conclude that a sulfur abundance of S/H = 3.5×10^{-6} can reproduce the observed abundance of CS, HCS^+, and H_2CO.

It is important to remember that models that include complex grain surface processes use numerous physical parameters, such as the adsorption energy, diffusion energy of absorbed species, the activation energy of the different hydrogenation reactions, and the desorption yield, which have large uncertainties. The results predicted by these models are highly dependent on the values used for these parameters. Providing observational results is crucial to constrain these parameters and benchmark the models.

6. Discussion

6.1. Observational evidence of different H_2CO formation mechanisms

The observations suggest that H_2CO is formed on the surface of dust grains at the PDR and is mostly formed in the gas-phase at the dense core. First, we found a different ortho-to-para ratio in each position: an equilibrium value of 3 was found at the dense core, while a lower out-of-equilibrium value of 2 was found at the PDR. Second, if H_2CO is formed on the grains, its spatial distribution is expected to resemble the spatial distribution of CH_3OH. However, the high-resolution PdBI maps show that the CH_3OH emission presents a minimum at the dense-core position, while H_2CO peaks at this position. The easiest interpretation is that 1) the photodesorption of both H_2CO and CH_3OH is inefficient at the dense core, therefore the ices remain depleted onto grains; and that 2) H_2CO is formed in the gas phase at this position. Indeed, the pure gas-phase model reproduces the H_2CO abundance at the dense core well. Moreover, fewer photons can photodesorb species at the dense core than are available at the PDR position. This way, gas-phase CH_3OH is present in an envelope around the dense core, while H_2CO is present in both the envelope and the dense core itself. This is consistent with the lower gas-density inferred from the radiative-transfer analysis of CH_3OH at the dense-core position.

Depletion of CH_3OH has also been observed in other dense cores. Tafalla et al. (2006) found that CH_3OH shows a dip in its emission at the center of the dense cores L1498 and L1517B. They concluded that the drop in emission corresponds to a real drop in column density, suggesting that CH_3OH freeze out onto grains at the center of these dense cores.

6.2. Comparison with other environments

H_2CO and CH_3OH have been detected in the Orion Bar, which is a more extreme case of a PDR (higher χ, $T_{\rm kin}$ and $T_{\rm dust}$). Leurini et al. (2010) estimated an abundance ratio $H_2CO/CH_3OH = 14-1400$ in the interclump medium ($n_{\rm H} \sim 10^4$ cm^{-3}) and $H_2CO/CH_3OH = 0.9-2.5$ in the denser clumps ($n_{\rm H} \sim 10^6$ cm^{-3}). Despite the large uncertainties and the fact that the clumpy medium was not resolved, they concluded that the abundance of methanol relative to formaldehyde decreases by at least one order of magnitude in the interclump medium in comparison to the dense clumps. Unlike the situation at the Orion Bar, we only found a small difference in the H_2CO/CH_3OH abundance ratio between the PDR and dense core in the Horsehead (H_2CO/CH_3OH is only twice as high in the PDR). This is probably due to the difference in the radiation field between the two sources ($\chi \simeq 10^4$ in the Orion Bar; $\chi = 60$ in the Horsehead). Hence, photodissociation of CH_3OH (which produces H_2CO) is more efficient in the Orion Bar, especially in the interclump medium, and the ratio of H_2CO/CH_3OH is thus higher. The H_2CO/CH_3OH abundance ratio we derive in the Horshead (0.9–2.3) is very similar to the one found in the dense clumps of the Orion Bar. These clumps are more protected from

the FUV photons and thus resemble more closely the conditions prevailing in the Horsehead. Indeed, $\chi/n \sim 100/10^4$ in the Horsehead, which is similar to the ratio found in the dense clumps of the Orion Bar ($\chi/n \sim 10^4/10^6$).

Maret et al. (2004, 2005) measured the formaldehyde and methanol abundances toward a sample of low-mass protostars. From these studies, an abundance ratio H_2CO/CH_3OH = 0.7–4.3 was found for the hot-corino region. In the low-mass starless cores, L1498 and L1517B, Tafalla et al. (2006) found H_2CO/CH_3OH = 1.1–2.2. These values are similar to the abundance ratio derived in the Horsehead. A lower abundance ratio was found in hot cores (H_2CO/CH_3OH = 0.13–0.28; Bisschop et al. 2007), and an even lower ratio was found in shocked gas in Galactic center clouds ($H_2CO/CH_3OH \sim 0.01$; Requena-Torres et al. 2006). In the diffuse medium, H_2CO is widely detected (e.g., Liszt et al. 2006), but methanol has not been detected, although it has been searched for by Liszt et al. (2008). They derived an upper limit for the CH_3OH column density, which translates into a lower limit for the abundance ratio of $H_2CO/CH_3OH \geq 12$.

6.3. Thermal and nonthermal desorption

In hot cores, hot corinos, and shocked regions the ices that were formed in the cold gas in the prestellar stage are completely sublimated into the gas-phase through thermal desorption and sputtering. The observed H_2CO and CH_3OH gas-phase abundances in these regions should therefore resemble the original ice composition. Observations of ices in the envelopes of low-mass protostars show strong variations of the CH_3OH ice abundance with respect to water ice (1%–30%; Boogert et al. 2008). In cold cores, a methanol ice abundance of 5%–12% relative to water has been found (Boogert et al. 2011). The variations in the CH_3OH ice abundance are caused by the different local physical conditions and thus reflect the variations in the evolutionary stages of these sources (Cuppen et al. 2009). The abundance of H_2CO ice has been more difficult to determine because it has been detected in just a few sources, and its stronger ice feature at 6 μm is blended with that of HCOOH (Öberg et al. 2011). A relatively constant H_2CO ice abundance of ~6% relative to water was found in low-mass protostars (Gibb et al. 2004; Boogert et al. 2008). This value seems to be independent of the CH_3OH ice abundance. From these detections, an ice abundance ratio $H_2CO/CH_3OH \simeq 0.2$–6.0 is obtained in low-mass protostars, which is consistent with the gas-phase abundance ratio found in hot corinos by Maret et al. (2004, 2005).

In cold cores and low-UV illumination PDRs, the ices are released through nonthermal processes, such as photodesorption. The H_2CO/CH_3OH ratio will therefore depend on the dust temperature and on the number of UV photons that will desorb the ices into the gas-phase. The CH_3OH photodesorption yield has been previously found to be $\sim 10^{-3}$ molecules per incident UV photon, similar to other species such as CO, CO_2, and H_2O (Öberg et al. 2009a–c). Although the CH_3OH photodesorption yield is uncertain, the one adopted in our model gives a CH_3OH abundance that is consistent with the observations. As discussed in Sect. 5.2, the predictions of chemical models including grain surface chemistry are highly dependent on the different physical parameters. Future laboratory studies, using different ice mixtures (similar to those observed in the ISM), will help to better understand the nonthermal desorption of ices into the gas phase and will hopefully provide precise values for the photodesorption yields and other parameters needed in the models.

7. Summary and conclusions

We have presented deep observations of CH_3OH lines toward the Horsehead PDR and its associated dense core, together with single-dish and interferometric observations of H_2CO and CH_3OH. In general, formaldehyde and methanol emission is extended, although there are a few differences. The CH_3OH emission presents a minimum at the dense-core position that is also seen in the lower angular resolution 30 m map, while H_2CO peaks at this position. From the high-resolution maps, we concluded that beam dilution of the single-dish deep integrations is marginal. This is in contrast with the model prediction of an abundance peak at the PDR position. We therefore confirm the H_2CO abundances inferred by Guzmán et al. (2011) and derived a similar CH_3OH abundance with respect to H ($\sim 10^{-10}$) in the PDR and dense-core position that is also similar to the observed abundance of H_2CO. We found that collisions with electrons are not important in determining the CH_3OH column density when the physical conditions of the gas are known. However, to determine the kinetic temperature and density of the gas, electron excitation should be taken into account. The inferred methanol E/A ratio is close to one in both the PDR and the dense-core position. The H_2CO/CH_3OH abundance ratio is 2.3 ± 0.4 in the PDR and 0.9 ± 0.1 in the dense core.

At the PDR, observations suggest that both H_2CO and CH_3OH are formed on the surface of dust grains and are subsequently released into the gas phase through photodesorption. Indeed, pure gas-phase chemical models predict H_2CO and CH_3OH abundances that are too low compared with what is inferred from the observations. At the dense core, on the other hand, the dominant formation mechanism differs for H_2CO and CH_3OH. H_2CO is mostly formed in the gas phase, while CH_3OH is formed on the grains. Indeed, a pure gas-phase model can reproduce the observed H_2CO abundance at this position, while it fails by ~5 orders of magnitude for CH_3OH. Moreover, the high-resolution PdBI maps show that CH_3OH is present in an envelope around the dense core, while H_2CO is present in both the envelope and the dense core itself. The result of different H_2CO formation mechanisms in the PDR and dense core are strengthened by the different ortho-to-para ratio inferred from the observations (o/p $\sim$ 2 in the PDR and the equilibrium value o/p ~ 3 in the dense core).

Acknowledgements. We thank the IRAM PdBI and 30 m staff for their support during the observations. We thank Simon Radford for his help during the CSO observations and data reduction. VG thanks support from the Chilean Government through the Becas Chile scholarship program. This work was also funded by grant ANR-09-BLAN-0231-01 from the French *Agence Nationale de la Recherche* as part of the SCHISM project. J.R.G. thanks the Spanish MINECO for funding support from grants AYA2012-32032, AYA2009-07304 and CSD2009-00038. J.R.G. is supported by a Ramón y Cajal research contract.

References

Bergman, P., Parise, B., Liseau, R., & Larsson, B. 2011, A&A, 527, A39
Bernstein, M. P., Dworkin, J. P., Sandford, S. A., Cooper, G. W., & Allamandola, L. J. 2002, Nature, 416, 401
Bisschop, S. E., Jørgensen, J. K., van Dishoeck, E. F., & de Wachter, E. B. M. 2007, A&A, 465, 913
Boogert, A. C. A., Pontoppidan, K. M., Knez, C., et al. 2008, ApJ, 678, 985
Boogert, A. C. A., Huard, T. L., Cook, A. M., et al. 2011, ApJ, 729, 92
Bottinelli, S., Ceccarelli, C., Williams, J. P., & Lefloch, B. 2007, A&A, 463, 601
Bottinelli, S., Boogert, A. C. A., Bouwman, J., et al. 2010, ApJ, 718, 1100
Brown, W. A., & Bolina, A. S. 2007, MNRAS, 374, 1006
Caselli, P., Keto, E., Bergin, E. A., et al. 2012, ApJ, 759, L37
Ceccarelli, C., Loinard, L., Castets, A., Tielens, A. G. G. M., & Caux, E. 2000, A&A, 357, L9
Cernicharo, J., Marcelino, N., Roueff, E., et al. 2012, ApJ, 759, L43

Codella, C., Ceccarelli, C., Lefloch, B., et al. 2012, ApJ, 757, L9
Cuppen, H. M., van Dishoeck, E. F., Herbst, E., & Tielens, A. G. G. M. 2009, A&A, 508, 275
Draine, B. T. 1978, ApJS, 36, 595
Faure, A., Gorfinkiel, J. D., & Tennyson, J. 2004, MNRAS, 347, 323
Fuchs, G. W., Cuppen, H. M., Ioppolo, S., et al. 2009, A&A, 505, 629
Garrod, R., Park, I. H., Caselli, P., & Herbst, E. 2006, Faraday Discuss., 133, 51
Garrod, R. T., Weaver, S. L. W., & Herbst, E. 2008, ApJ, 682, 283
Geppert, W. D., Hamberg, M., Thomas, R. D., et al. 2006, Faraday Discuss., 133, 177
Gerin, M., Goicoechea, J. R., Pety, J., & Hily-Blant, P. 2009, A&A, 494, 977
Gibb, E. L., Whittet, D. C. B., Schutte, W. A., et al. 2000, ApJ, 536, 347
Gibb, E. L., Whittet, D. C. B., Boogert, A. C. A., & Tielens, A. G. G. M. 2004, ApJS, 151, 35
Goicoechea, J. R., Pety, J., Gerin, M., et al. 2006, A&A, 456, 565
Goicoechea, J. R., Compiègne, M., & Habart, E. 2009a, ApJ, 699, L165
Goicoechea, J. R., Pety, J., Gerin, M., Hily-Blant, P., & Le Bourlot, J. 2009b, A&A, 498, 771
Gratier, P., Pety, J., Guzmán, V., et al. 2013, A&A, 557, A101
Green, S. D., Bolina, A. S., Chen, R., et al. 2009, MNRAS, 398, 357
Guzmán, V., Pety, J., Goicoechea, J. R., Gerin, M., & Roueff, E. 2011, A&A, 534, A49
Habart, E., Abergel, A., Walmsley, C. M., Teyssier, D., & Pety, J. 2005, A&A, 437, 177
Hily-Blant, P., Teyssier, D., Philipp, S., & Güsten, R. 2005, A&A, 440, 909
Itikawa, Y. 1971, J. Phys. Soc. Jpn., 30, 835
Jørgensen, J. K., Schöier, F. L., & van Dishoeck, E. F. 2005, A&A, 437, 501
Le Petit, F., Nehmé, C., Le Bourlot, J., & Roueff, E. 2006, ApJS, 164, 506
Leurini, S., Schilke, P., Menten, K. M., et al. 2004, A&A, 422, 573
Leurini, S., Parise, B., Schilke, P., Pety, J., & Rolffs, R. 2010, A&A, 511, A82
Liszt, H. S., Lucas, R., & Pety, J. 2006, A&A, 448, 253
Liszt, H. S., Pety, J., & Lucas, R. 2008, A&A, 486, 493
Mangum, J. G., & Wootten, A. 1993, ApJS, 89, 123
Mangum, J. G., Darling, J., Henkel, C., & Menten, K. M. 2013, ApJ, 766, 108
Maret, S., Ceccarelli, C., Caux, E., et al. 2004, A&A, 416, 577
Maret, S., Ceccarelli, C., Tielens, A. G. G. M., et al. 2005, A&A, 442, 527
Muñoz Caro, G. M., Meierhenrich, U. J., Schutte, W. A., et al. 2002, Nature, 416, 403
Muñoz Caro, G. M., Jiménez-Escobar, A., Martín-Gago, J. Á., et al. 2010, A&A, 522, A108
Müller, H. S. P., Thorwirth, S., Roth, D. A., & Winnewisser, G. 2001, A&A, 370, L49
Öberg, K. I., Fuchs, G. W., Awad, Z., et al. 2007, ApJ, 662, L23
Öberg, K. I., Boogert, A. C. A., Pontoppidan, K. M., et al. 2008, ApJ, 678, 1032
Öberg, K. I., Garrod, R. T., van Dishoeck, E. F., & Linnartz, H. 2009a, A&A, 504, 891
Öberg, K. I., Linnartz, H., Visser, R., & van Dishoeck, E. F. 2009b, ApJ, 693, 1209
Öberg, K. I., van Dishoeck, E. F., & Linnartz, H. 2009c, A&A, 496, 281
Öberg, K. I., Boogert, A. C. A., Pontoppidan, K. M., et al. 2011, ApJ, 740, 109
Parise, B., Castets, A., Herbst, E., et al. 2004, A&A, 416, 159
Parise, B., Ceccarelli, C., Tielens, A. G. G. M., et al. 2006, A&A, 453, 949
Penzias, A. A., & Burrus, C. A. 1973, ARA&A, 11, 51
Pety, J. 2005, in SF2A-2005: Semaine de l'Astrophysique Française, eds. F. Casoli, T. Contini, J. M. Hameury, & L. Pagani, 721
Pety, J., & Rodríguez-Fernández, N. 2010, A&A, 517, A12
Pety, J., Goicoechea, J. R., Hily-Blant, P., Gerin, M., & Teyssier, D. 2007, A&A, 464, L41
Pickett, H. M., Poynter, R. L., Cohen, E. A., et al. 1998, J. Quant. Spec. Rad. Transf., 60, 883
Pontoppidan, K. M., Boogert, A. C. A., Fraser, H. J., et al. 2008, ApJ, 678, 1005
Pound, M. W., Reipurth, B., & Bally, J. 2003, AJ, 125, 2108
Rabli, D., & Flower, D. R. 2010, MNRAS, 406, 95
Requena-Torres, M. A., Martín-Pintado, J., Rodríguez-Franco, A., et al. 2006, A&A, 455, 971
Rodriguez-Fernandez, N., Pety, J., & Gueth, F. 2008, Single-dish observation and processing to produce the short-spacing information for a millimeter interferometer, Tech. Rep., IRAM Memo 2008-2
Sakai, N., Ceccarelli, C., Bottinelli, S., Sakai, T., & Yamamoto, S. 2012, ApJ, 754, 70
Sutton, E. C., Peng, R., Danchi, W. C., et al. 1995, ApJS, 97, 455
Tafalla, M., Santiago-García, J., Myers, P. C., et al. 2006, A&A, 455, 577
Tafalla, M., Santiago-García, J., Hacar, A., & Bachiller, R. 2010, A&A, 522, A91
Tielens, A. G. G. M., & Allamandola, L. J. 1987, in Interstellar Processes, eds. D. J. Hollenbach, & H. A. Thronson, Jr., Astrophys. Space Sci. Lib., 134, 397
Tielens, A. G. G. M., & Whittet, D. C. B. 1997, in IAU Symp. 178, ed. E. F. van Dishoeck, 45
van der Tak, F. F. S., Black, J. H., Schöier, F. L., Jansen, D. J., & van Dishoeck, E. F. 2007, A&A, 468, 627
Vinodkumar, M., Limbachiya, C., Barot, A., & Mason, N. 2013, Phys. Rev. A, 87, 012702
Watanabe, N., & Kouchi, A. 2002, ApJ, 571, L173
Watanabe, N., Nagaoka, A., Shiraki, T., & Kouchi, A. 2004, ApJ, 616, 638